AGU PUBLICATIONS

JGR

Journal of Geophysical Research: Solid Earth

RESEARCH ARTICLE
10.1002/2017JB014115

This article is a companion to *Massiot et al.* [2017] doi:10.1002/2017JB014121.

Key Points:
- Objective fracture set delineation of BHTV log data using clustering algorithms
- Assessment of sampling bias and BHTV log quality for the statistical analysis of fracture attributes
- Maximum likelihood estimations of fracture attributes using truncated probability distributions

Supporting Information:
- Supporting Information S1

Correspondence to:
C. Massiot,
c.massiot@gns.cri.nz

Citation:
Massiot, C., J. Townend, A. Nicol, and D. D. McNamara (2017), Statistical methods of fracture characterization using acoustic borehole televiewer log interpretation, *J. Geophys. Res. Solid Earth*, *122*, 6836–6852, doi:10.1002/2017JB014115.

Received 20 FEB 2017
Accepted 20 MAY 2017
Published online 26 AUG 2017

Statistical methods of fracture characterization using acoustic borehole televiewer log interpretation

Cécile Massiot[1,2], John Townend[1], Andrew Nicol[3], and David D. McNamara[2,4]

[1]School of Geography, Environment, and Earth Sciences, Victoria University of Wellington, Wellington, New Zealand, [2]GNS Science, Avalon, Lower Hutt, New Zealand, [3]Department of Geological Sciences, University of Canterbury, Christchurch, New Zealand, [4]Earth and Ocean Sciences, School of Natural Sciences, National University of Ireland, Galway, Galway, Ireland

Abstract Acoustic borehole televiewer (BHTV) logs provide measurements of fracture attributes (orientations, thickness, and spacing) at depth. Orientation, censoring, and truncation sampling biases similar to those described for one-dimensional outcrop scanlines, and other logging or drilling artifacts specific to BHTV logs, can affect the interpretation of fracture attributes from BHTV logs. *K*-means, fuzzy *K*-means, and agglomerative clustering methods provide transparent means of separating fracture groups on the basis of their orientation. Fracture spacing is calculated for each of these fracture sets. Maximum likelihood estimation using truncated distributions permits the fitting of several probability distributions to the fracture attribute data sets within truncation limits, which can then be extrapolated over the entire range where they naturally occur. Akaike Information Criterion (AIC) and Schwartz Bayesian Criterion (SBC) statistical information criteria rank the distributions by how well they fit the data. We demonstrate these attribute analysis methods with a data set derived from three BHTV logs acquired from the high-temperature Rotokawa geothermal field, New Zealand. Varying BHTV log quality reduces the number of input data points, but careful selection of the quality levels where fractures are deemed fully sampled increases the reliability of the analysis. Spacing data analysis comprising up to 300 data points and spanning three orders of magnitude can be approximated similarly well (similar AIC rankings) with several distributions. Several clustering configurations and probability distributions can often characterize the data at similar levels of statistical criteria. Thus, several scenarios should be considered when using BHTV log data to constrain numerical fracture models.

1. Introduction

Defining the geometries of fracture systems in reservoirs requires a robust delineation of individual fracture sets of similar orientation and of their geometrical variability. Each fracture set can result from a specific geological event and/or a different process [*Bonnet et al.*, 2001; *Dezayes et al.*, 2015]. Different fracture sets can have different geometrical (e.g., size, aperture, and density) and mineralogical (infill material and quantity) properties and thus may have different impacts on the hydrology of the system [*Agosta et al.*, 2010]. In addition, numerical models of fracture systems and their associated fluid pathways in reservoirs can be constrained by the assumed probability distributions of aperture, length, and density of each fracture set [e.g., *Dershowitz and Einstein*, 1988; *Bonneau et al.*, 2013], which thus need to be assessed carefully. Analogue outcrop studies can provide extensive and detailed fracture system characterization but may not be directly comparable to conditions in reservoirs. On the contrary, fracture data measured in boreholes are typically sparse and affected by artifacts but directly reflect structural and hydrological properties in reservoirs.

Acoustic borehole televiewer (BHTV) logs provide an image of the inside of a borehole by measuring the acoustic amplitude and return time of an ultrasonic signal emitted by the logging tool [*Zemanek et al.*, 1970; *Poppelreiter et al.*, 2010]. Analysis of these logs yields continuous samples of fractures intersecting the borehole, including their position, orientation, and thickness. In general, BHTV logs cannot discriminate between open and closed fractures (unless the fractures are infilled with high acoustic impedance minerals such as quartz [*Milloy et al.*, 2015]), so we use the term "fracture" in the general sense of discontinuity and refer to the distance between the two fracture walls as "thickness." Image logs, such as BHTV logs, are particularly useful in boreholes where continuous oriented drill cores are not available, as is commonly the case in hydrocarbon and geothermal reservoirs. Image logs are subject to similar sampling biases to 1-D outcrop scanlines, as well

as biases related to drilling and logging artifacts [e.g., *Lofts and Bourke*, 1999] that can decrease image quality locally. All biases need to be evaluated and incorporated into the statistical analysis of fracture geometries.

The classical method for delineating fracture sets is to plot fracture orientations on hemispherical projections (stereonets) and contour the projected poles to fracture planes by their areal density, yielding a "Fisher" density. This method is intuitive and straightforward to apply, thanks to stereonet software packages. However, the delineation of fracture sets from these contours is subjective and may vary between data analysts. Cluster analysis of fracture orientation provides a transparent means of separating fracture orientation data into sets, as proposed by *Shanley and Mahtab* [1976]. Agglomerative, *K*-means, and fuzzy *K*-means clustering have been used to analyze orientation data derived from scanline measurements, predominantly for engineering purposes [e.g., *Hammah and Curran*, 1998, 1999; *Zhou and Maerz*, 2002; *Tokhmechi et al.*, 2011; *Li et al.*, 2014] but rarely for reservoir borehole data interpretation.

Fracture attributes (e.g., thickness, spacing, and length) have been shown to variously follow power law, exponential, gamma, lognormal, and power-exponential distributions [see *Bonnet et al.*, 2001, and references therein; *Torabi and Berg*, 2011]. Faults commonly exhibit power law spacings, although this may partially reflect sampling bias and the mixing of different fracture sets [*Gillespie et al.*, 1993; *Nicol et al.*, 1996]. On the contrary, joint spacing in layered systems is usually best approximated by distributions with characteristic scales such as lognormal, gamma, or exponential distributions [*Gillespie et al.*, 1993; *Schöpfer et al.*, 2011]. In consequences, determination of the distribution form and parameters of fracture attributes is not only necessary for constraining reservoir-scale fracture models [*Berkowitz*, 2002] but also informs on the nature of fracture systems. Distributions are commonly evaluated with linear regressions, with power law exponents estimated using linear regression to the cumulative density function (CDF) of observations in doubly logarithmic axes ("log-log" plots, see *McCaffrey et al.* [2003] for example). However, this method is not mathematically robust and does not unambiguously demonstrate that the observations are power law [*Clauset et al.*, 2009]. The maximum likelihood estimation (MLE) method is preferred to least squares fitting for estimating which probability distribution and associated parameters best fit a set of data [*Laslett*, 1982; *Villaescusa and Brown*, 1992; *Clauset et al.*, 2009]. The MLE method estimates values for the parameters of a given distribution that maximize a likelihood function, i.e., finds the parameter set that makes the observed data most likely.

This paper details methods with which to discriminate between fracture sets of different orientation using clustering algorithms and to evaluate the probability distribution and parameters of fracture attributes (thickness, spacing) via maximum likelihood estimations. While these methods are generally applicable to 1-D data sets, this paper addresses fracture data sets obtained from BHTV logs and their specific limitations, which have not been fully considered to date. Fractures used as examples are interpreted from three BHTV logs acquired in the high-temperature Rotokawa Geothermal field, Taupo Volcanic Zone, New Zealand. The geologic implications of this statistical analysis are presented in a companion paper [*Massiot et al.*, 2017]. Our analysis includes consideration of sampling biases in BHTV logs, a strategy for accommodating varying BHTV log quality, and qualitative estimation of the size and range of a data set required to fully constrain the distribution fitting. Similar analysis can be conducted on other fracture attributes (e.g., length) and with other linear sampling methods (e.g., scanlines) taking into consideration relevant factors affecting those data.

2. Data

The fracture data set utilized in this paper was derived from three BHTV logs acquired in boreholes RK18L2, RK30L1, and RK32 in the high-temperature Rotokawa geothermal field, located in the Taupo Volcanic Zone, New Zealand. These data were described by *McNamara et al.* [2015], and here measurement of fracture thickness has been further improved. The three boreholes heads are located within an area of 1 km^2; the depth intervals, and number of fractures identified in each well, are detailed in Table 1. The BHTV logs were acquired with an ABI-85, a high-temperature logging tool able to operate at up to 300°C [*Ásmundsson et al.*, 2014]. The boreholes intersect several lithologies; here we focus on the andesitic formations which form the main part of the deep reservoir [*McNamara et al.*, 2016]. Fractures are dominantly steeply dipping (> 60° dip) and striking parallel to the azimuth of maximal horizontal compressive stress (S_{Hmax}) which varies between NNE-SSW and ENE-WSW (Figure A1a), and reflects the regional normal faulting in the Taupo Rift [*Seebeck et al.*, 20142014; *McNamara et al.*, 2015, 2016].

Fractures were identified in the BHTV logs using the Recall™ 5.3 software following the methods discussed by *Massiot et al.* [2015]. Borehole deviations of up to 30° from vertical were accounted for during log processing,

Table 1. Borehole Trajectory and Number of Fractures for Each Borehole, as Described by *McNamara et al.* [2015][a]

		RK18L2	RK30L1	RK32	Combined
Depth range (m)		995–1385; 1710–2255	1660–2060	1712–2639	
Average deviation		23°±2°	24°±1°	20°±1°	
Average azimuth		100°±16°	220°±4°	314°±3°	
Number of fractures	Total	358	321	539	1218
	Quality 3–5	324	276	533	1133
	Outliers	71	67	83	221

[a]Depth is measured along the boreholes. *Total*, total number of fractures; *Quality 3–5*, number of fractures in BHTV log of intermediate quality, ranks 3-5; *Outliers*, number of outlier fractures in zones of moderate quality with <1% Fisher density not used for orientation clustering (see text for details).

with the orientations presented here referenced to geographic north and horizontal. In total, 1218 fractures were identified over 2073.5 m of BHTV logs (Figure 1 and Table 1); they are described in terms of their location along the borehole, orientation, thickness, and descriptive characteristics (e.g., high or low acoustic amplitude and cross-cutting relationships with nearby fractures). The apparent fracture thickness measured at the borehole wall has been converted to the true thickness that would be measured perpendicular to the fracture walls [*Barton and Zoback*, 1992; *Massiot et al.*, 2015]. The apparent spacing between neighboring fractures of the same set resolved in the BHTV logs has been measured along the borehole trajectory and was converted to the fracture-normal spacing [*Priest*, 1993].

The BHTV logs acquired at Rotokawa commonly have only partial coverage of the borehole and contain a number of logging- and drilling-induced artifacts that decrease the image quality [*Lofts and Bourke*, 1999; *McNamara et al.*, 2015]. Image quality has been qualitatively assigned using a five-class ranking scheme [*Massiot et al.*, 2015]. Fracture detection can be hindered in zones of low- or very poor-quality images, which may adversely affect the statistical analysis of fracture attributes, particularly the spacing. Orientation analysis has been performed for each borehole individually and the data combined, after correction for orientation

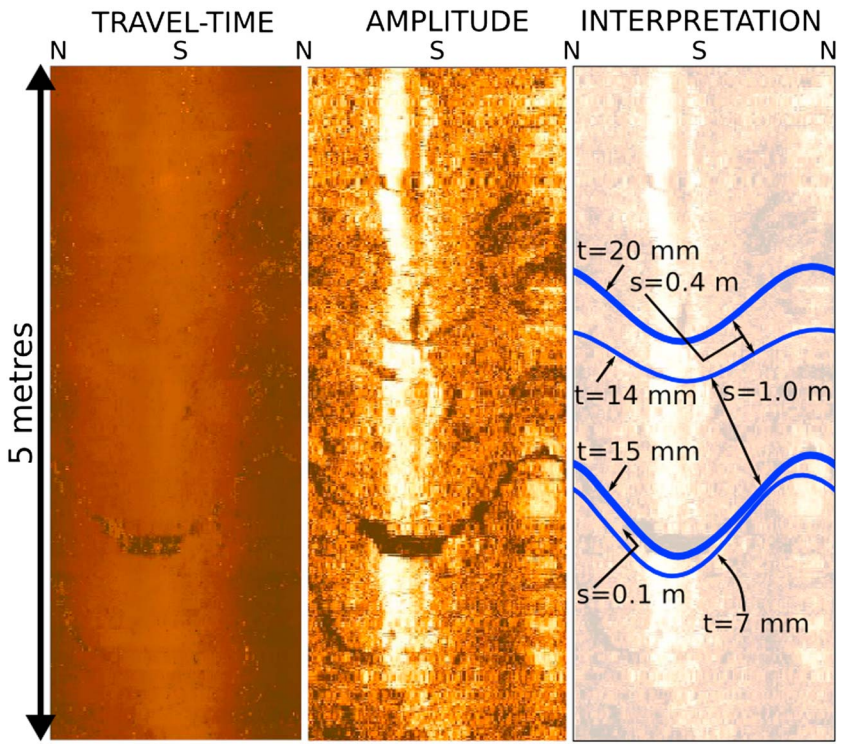

Figure 1. Example of a BHTV log with travel time and amplitude oriented images showing various fracture thickness ("t") and spacing ("s") values.

sampling bias [*Terzaghi*, 1965; *Massiot et al.*, 2015]. Other biases associated with incomplete detection of small attribute values, and the low probability of occurrence of high-attribute values, have also been addressed in this paper.

3. Fracture Set Orientation Clustering

3.1. Cluster Analysis Methods

Fracture sets are commonly identified on stereonets using Fisher or Kamb contours, but discrimination between fracture sets is not always clear where high-density zones overlap. Clustering algorithms divide a data set into groups (clusters) of observations that are similar to each other. In such algorithms, a "dissimilarity" metric must be selected to describe how far apart data points are from each other. The metric summarizes all relevant aspects of similarity into a single measure. Here we use the acute angle between the normals of each pair of fractures as the dissimilarity metric between fracture orientations. Two subparallel, steeply dipping ($> 80°$) fractures may have different dip directions ($\pm 180°$) but small acute angle between their normals and may thus belong to the same set. Two types of cluster analysis are used in this paper: partitional, based on a prior specification of the desired number of clusters (K); and hierarchical, which constructs a hierarchy between one and n nested clusters, n being the number of observations.

K-means clustering is a partitional method that assigns each data point to one of K clusters [*James et al.*, 2013]. The assignment is an iterative process that minimizes a sum of dissimilarities between the centroid of the cluster and each data point within the cluster. Data points are reallocated between clusters until an optimal configuration is reached. This process is computationally efficient, but issues can result from the selection of initial centroid locations, which can lead to nonunique selection of a local minimum instead of the global minimum of the sum of dissimilarities, and also to the possible generation of empty clusters [*James et al.*, 2013]. Comparing clustering results using different initial centroids mitigates these risks. The K-means method is most successful when applied to globular clusters of similar sizes and densities, without too many outliers, and to subclusters. Defining the optimal number of clusters for a data set is non trivial. Good clusterings have a low cohesion, where objects are close to each other within their cluster, and a high separation, where clusters are distinct from each other (Figure 2b). The silhouette value combines the cohesion and separation values [*Reynolds et al.*, 2006]. For each data point i, the silhouette value is calculated as

$$s(i) = \frac{b(i) - a(i)}{\max(a(i), b(i))} \tag{1}$$

where $a(i)$ is the average dissimilarity of the data point i with all other data within the same cluster (cohesion), and $b(i)$ is the lowest average dissimilarity of i to any cluster of which the ith datum is not a member (separation). A value of $s(i)$ close to 1 indicates that the datum is appropriately clustered. When testing several input numbers of clusters, the optimal cluster number is found when the average $s(i)$ for the entire data set is maximized.

The fuzzy K-means approach allows the data points to belong to several clusters at once, with varying degrees of membership to each cluster, which is appropriate when clusters are overlapping or not compact [*Zadeh*, 1965]. For example, a data point can belong 20% to one cluster and 80% to a second cluster; overall, the data point belongs predominantly to the latter cluster (Figure 2d). A clustering result that maximizes the membership level for each data point to their dominant cluster is thus desirable and is achieved here by calculating the median of each data point's highest membership level (80% for the data point in this example). A high median membership indicates a well-separated clustering result.

The agglomerative hierarchical clustering method, also called *bottom-up*, starts with each observation constituting a cluster and successively merges the two nearest clusters until only one large cluster remains containing all observations [*James et al.*, 2013] (Figure 2f). Thus, each step j of the agglomerative process contains $(n - j + 1)$ clusters. In contrast with the K-means clustering, agglomerative hierarchical clustering is not affected by the initialization step and local minima. However, the data point merges are definitive and the process can produce unstable clusters when data points are allocated early to a cluster that they would not belong to if they had been allocated later. Agglomerative clustering is also more computationally expensive than the K-means process. The sequence of agglomerative clustering can be visualized on a dendogram, a graphical representation of the nested clusters (Figure 2e). Dendograms represent the successive grouping of subclusters until the entire data set belongs to a single cluster: observations that are grouped early, near the

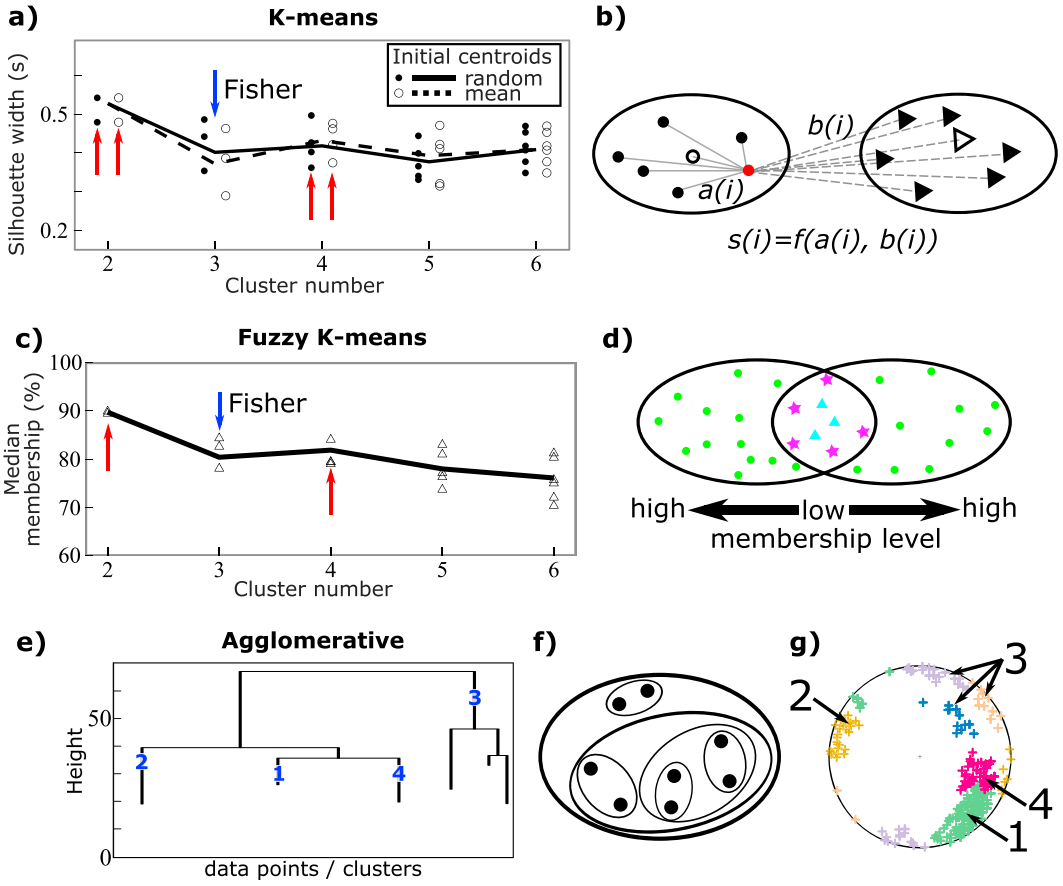

Figure 2. Evaluation of the optimal number of clusters for borehole RK30L1. The best clusterings are indicated by the underlying arrows, and the configuration is interpreted from Fisher contours by overlying arrows. (a) *K*-means: average silhouette width for each cluster (dots) and average of the average silhouette widths (line) for each number of clusters, with either random initial centroids or located at the mean orientation of the fracture set. (b) Synthetic *K*-means clustering with silhouette calculation as a function of cohesion and separation; the centroids of each clusters are open symbols. (c) Fuzzy *K*-means: median membership level for each cluster (triangles) and overall median membership level (line) for each number of clusters. (d) Synthetic fuzzy *K*-means of overlapping clusters with varying membership levels. (e) Dendogram of the agglomerative clustering, with the levels at which each of the four main fracture sets emerge. (f) Synthetic representation of successive agglomeration of data points or clusters. (g) Stereonet showing the agglomerative clustering result and associated cluster numbers (poles to plane, lower hemisphere Schmidt projection). Evaluative plots for other boreholes and the combined data set are in Appendix A. See text for explanations about separation, cohesion, and membership levels and Figure 3 for stereonets representing the Fisher and *K*-means clustering results.

bottom of the dendogram, are similar to each other, whereas observations that fuse later (close to the top) are more distinct from each other. A single dendogram can be used to obtain the partitioning of the data set in any desired number of clusters.

3.2. Fracture Set Delineation Example

To estimate the number of clusters best characterizing the fracture data sets and to assign each data point to a cluster, the fracture orientations are first analyzed using Fisher density contours on a stereonet (presented for borehole RK30L1 in Figure 3a). The loci of poles to undersampled fracture planes subparallel to the borehole are plotted as a shaded series of great circles. The fracture orientations are then clustered using *K*-means, fuzzy *K*-means, and agglomerative methods, for 2 to 6 clusters using the *pam*, *fanny*, and *agnes* functions in *R*, respectively [*R Core Team*, 2015]. Outliers, defined as having <1% Fisher density, were removed from the data set prior to the cluster analysis. As suggested by *K*-means theory [*James et al.*, 2013], tests run with outliers did not provide satisfying results. In such cases, both gently (< 40°) and steeply (> 70°) dipping fractures of similar dip direction were grouped in the same cluster, a result inconsistent with both Fisher contours analysis and the normal faulting regime at Rotokawa, where steeply dipping fractures are associated with normal faults.

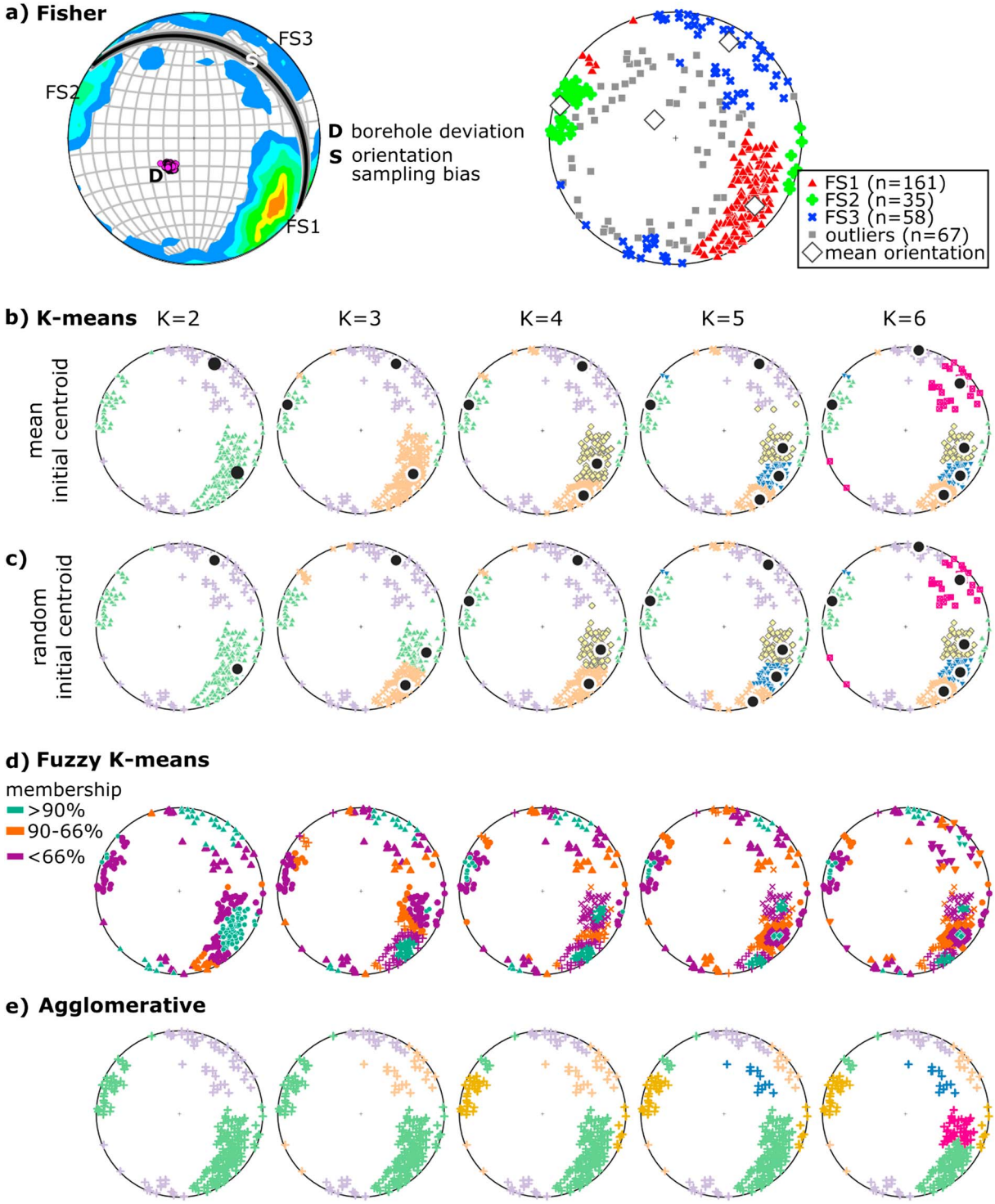

Figure 3. Example of fracture orientation analysis for borehole RK30L1 (n = 321). (a) Fisher contour and pole to planes with the resulting delineation comprising three fracture sets and outliers. (b) K-means clusters with the initial centroid specified at the mean orientation of the fracture sets, with 2 to 6 clusters (K). The centroid of each cluster is noted as a black dot. (c) K-means clusters with random initial centroids. (d) Fuzzy K-means clustering, colors indicate the membership level (input membership component is 1.5). (e) Agglomerative clustering. The colors in Figures 3b, 3c, and 3e are arbitrarily affected to each cluster, and stereonets displayed with increasing number of clusters from left (K = 2) to right (K = 6). Similar figures for the two other boreholes and the combined data set are available in the supporting information.

Each *K*-means clustering is made with two types of initial centroids: (1) imposed initial centroids located at the mean orientation of the fracture sets defined from Fisher contours (Figure 3b) and (2) randomly allocated centroids (Figure 3c). Fuzzy *K*-means clustering analysis highlights which fractures tend to lie between clusters (Figure 3d). The dendogram of the agglomerative clustering is presented for the six highest-level clusters, i.e., corresponding to between 2 and 6 clusters (Figure 2e). The lower part of the diagram, which includes all input data points, has been removed for clarity.

For configurations with two clusters, the results of *K*-means and agglomerative clusterings are similar to the sets defined from Fisher contours (see Figures 2 and 3 for example in borehole RK30L1; results for other boreholes are in Appendix A). With more than two clusters, the *K*-means and agglomerative clusterings yield different results. The optimal number of clusters for each data set is selected based on the highest average silhouette width of the *K*-means clustering and the highest median membership levels of the fuzzy *K*-means clustering (Figures 2a and 2c). For borehole RK30L1, the configurations with two and four clusters are the best clusterings, contrary to the three-cluster allocation interpreted from Fisher contours. The decrease in median membership for configurations with more than four clusters suggests that configurations with more clusters are unlikely. In addition, the statistical analysis of fracture attributes requires a sufficient number of fractures per set (see section 4.5), which is not the case for configurations with more than four clusters and thus not desirable.

The choice of initial centroids of the *K*-means algorithm influences the clustering results for individual boreholes but not for the combined data set containing more data points (Appendix A and Figure A1). Tests performed with several sets of randomly selected initial centroids yielded similar results. The use of random initial centroids is preferred to the imposed initial centroids, because they produce similar or higher mean silhouette widths than when the initial centroids are imposed at the mean orientation of each fracture set.

The dendogram of the agglomerative clustering provides additional insights into how well the clusters are separated and potential subclusters within the four fracture sets identified in this study. In borehole RK30L1, fracture set 3 is distinct from the combination of fracture sets 1, 2, and 4, as they are the last groups to be agglomerated; fracture sets 1 and 4, agglomerated early, are quite similar and may form subclusters (Figure 2e).

4. Fracture Attribute Probability Distribution Analysis

4.1. Sampling Biases

As in the case with 1-D scanline outcrop measurements, fracture data interpreted from BHTV logs are subject to resolution limits and sampling biases [*Laslett*, 1982; *Barton and Zoback*, 1992; *Pickering et al.*, 1995; *Nicol et al.*, 1996]. Small fracture thickness and spacing values are only partially recorded close to the resolution limit of the data set ("left-hand truncation"); conversely, high values may not be recorded because they are rare and may exceed the capacity of the measuring technique used to record them ("right-hand truncation"). The probability distribution of fracture attributes measured on the BHTV logs is thus estimated by fitting truncated distributions between truncation limits (scale range) within which all fractures are deemed to have been sampled. Truncated distributions are conditional distributions that result from restricting the domain of validity of a probability density function. The resulting distribution form and parameters fitted to a truncated data set can then be extrapolated to estimate the distribution of values beyond truncation limits.

At Rotokawa, fractures thinner than the BHTV log resolution of ~5 mm cannot be detected, except in rare cases where there is a large acoustic impedance contrast between the fracture and the host lithology. Histograms of fracture thickness indicate a paucity of fractures <8 mm thick in boreholes RK18L2 and RK30L1 and <9 mm in borehole RK32 (Figure 4a). Therefore, 9 mm is used as the left-hand truncation limit for fracture thickness. The right-hand truncation limit in BHTV logs is difficult to determine because it arises from a paucity of thick fractures rather than their incomplete detection by the tool. In addition, it is possible that rare fractures exceeding 30 mm thickness comprise several closely spaced fractures not resolved individually on the BHTV log ("censoring"). *Zuquim and Rowland* [2013] reported that extensional fractures in a paleo-hydrothermal system hosted in lava flows in the Coromandel area, north of the Taupo Volcanic Zone, were typically up to 30 mm thick, with some fractures up to a few hundred millimeters thick. Similarly, analysis of 3000 fractures in continuous cores from the Soultz geothermal reservoir found the thickest fracture to be 250 mm thick (a quartz vein), but that fractures exceeding 10 mm in thickness were rare [*Genter and Traineau*, 1996]. Overall, we consider

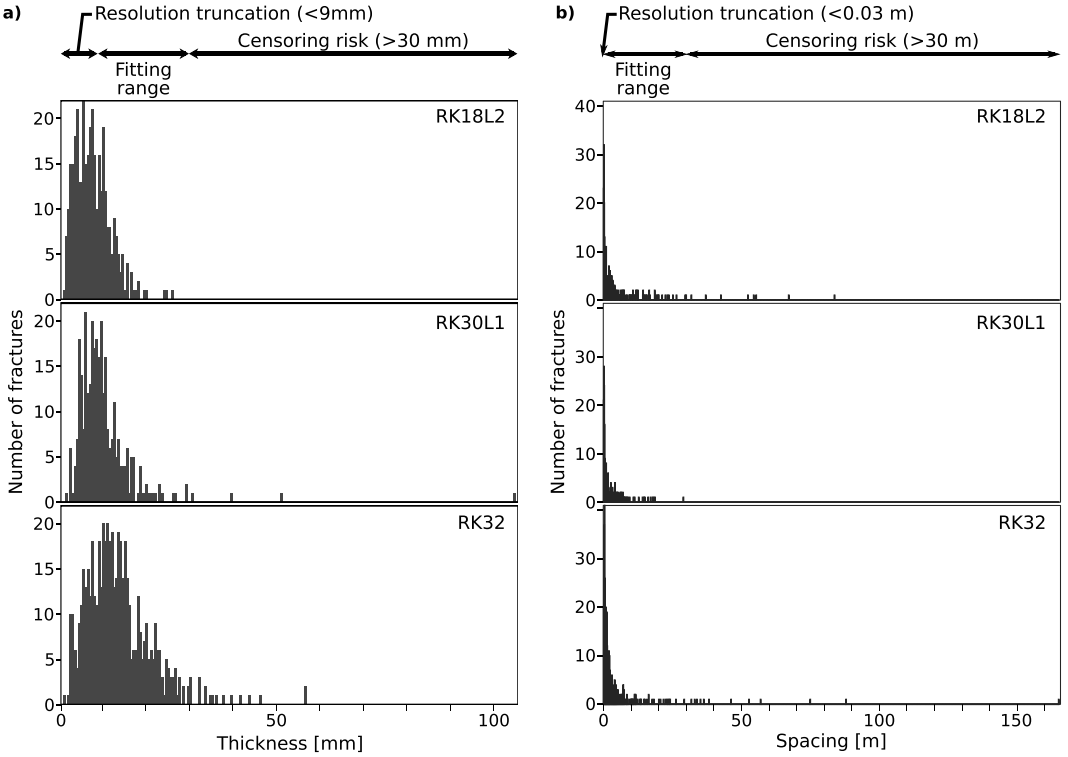

Figure 4. Histogram and sampling bias limits for (a) fracture thickness and (b) spacing for wells RK18L2, RK30L1, and RK32. Fracture spacing values from each fracture sets are superimposed in Figure 4b.

the 9–30 mm range of fracture thickness to be fully sampled in the BHTV logs acquired at Rotokawa; this range is analogous to that used in a similar study at Cajon Pass, U.S.A. [*Barton and Zoback*, 1992].

The left-hand truncation limit for the fracture spacing analysis is estimated to be 30 mm, based on the low probability of closely spaced fractures (i.e., <30 mm) being resolved by the BHTV log, and the right-hand limit is set at 30 m due to the scarcity of fractures with larger spacings (Figure 4b).

4.2. Effects of BHTV Log Quality

We consider the BHTV logs to sample most fractures in zones of quality ranking ≥3, as defined by *Massiot et al.* [2015]. Indeed, the small number of fractures in the two lowest-quality ranking zones (1 and 2) is interpreted to be due to incomplete sampling of fractures and, as a consequence, analysis of fracture spacing within these zones was not completed. Fracture detection is best in zones of high-quality rankings (4 and 5), but these zones are mostly <20 m long, preventing the evaluation of large spacings (i.e., >10 m). In addition, there can be too few data points in zones of high-quality ranking (4 and 5) for statistical analysis (14 points in zones of ranking 4 and 5 for fracture set 2 in borehole RK18L2, compared to 118 in zones of ranking 3-5; Figure 5b). The cumulative density functions (CDFs) of fracture spacing in zones of high-quality rankings (4 and 5) are similar to those of intermediate and high-quality ranking (3–5; Figure 5). As a result, statistical analyses of fracture spacing in zones of both intermediate and high quality will provide similar results to those made in zones of high quality, but with higher confidence in the results as there are more data points.

At Rotokawa, where 50% of the BHTV logs are of intermediate quality (rank 3), the statistical analysis of fracture spacing in zones of ranks 3–5 thus represents a good compromise between (1) a sufficient log quality allowing the sampling of most of the fractures that can be detected by the BHTV log and (2) sufficient length of continuous sections of log to sample large spacings.

4.3. Maximum Likelihood Estimation Using Truncated Distributions

Five probability distributions are commonly used to describe fracture attributes such as thickness and spacing: exponential, gamma, lognormal, power law, and power exponential (Table B1) [*Gillespie et al.*, 1993; *Bonnet et al.*, 2001, and references therein]. All these distributions have characteristic scales, except for the power law which is scale invariant.

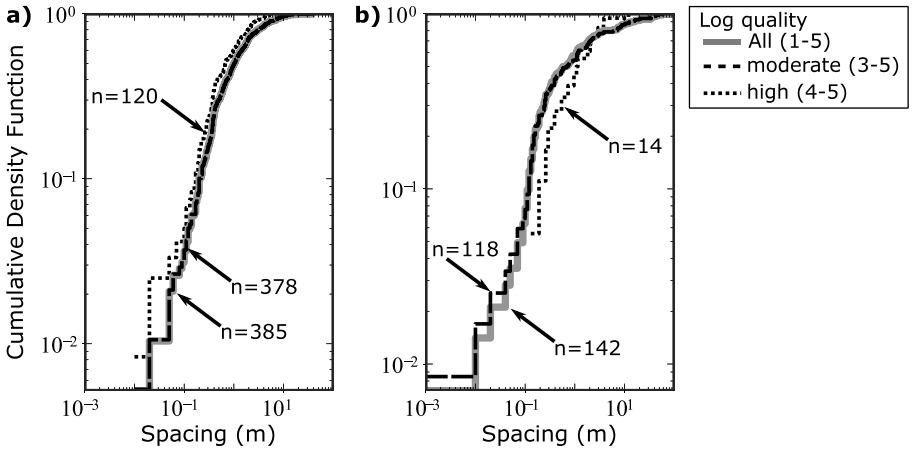

Figure 5. Cumulative density functions of fracture spacing with fractures in all BHTV log quality zones (rank 1–5), in intermediate quality zones (rank 3–5), and in moderate to good BHTV log quality zones only (rank 4 and 5). (a) Fracture set 1 in borehole RK32 (the curves for all and moderate quality ranks plot on top of each other). (b) Fracture set 2 in borehole RK18L2. *n* is the number of data points in each subset.

Probability distributions are fitted to the fracture thickness and spacing data interpreted from BHTV logs using the Generalized Additive Models for Location Scale and Shape library (GAMLSS) [*Stasinopoulos and Rigby*, 2007] (Table B1). This statistical modeling framework implemented in *R* uses the maximum likelihood estimation (MLE) method, which provides robust estimators by maximizing the likelihood function of the considered distribution [*Newman*, 2005; *Guerriero et al.*, 2011]. GAMLSS can be used to evaluate numerous distributions, which can all be truncated. The power law distribution is evaluated in GAMLSS with a Pareto type II distribution. Contrary to a power law distribution, the Pareto distribution does not appear as a straight line on log-log plots, but its form and coefficients are directly related to a power law under certain conditions (satisfied for thickness and spacing at Rotokawa; Table B1). The power law exponent is also fitted by MLE independently from GAMLSS [*Clauset et al.*, 2009, and references therein] (Table B1). For reference, the power law exponent is also evaluated with a least squares regression on log-log plots, although this is not mathematically robust [*Pickering et al.*, 1995; *Newman*, 2005].

Given a set of distributions fitted to a data set, the best fitting distribution amongst the set of distributions investigated is the one with the lowest Akaike Information Criterion (AIC) [*Akaike*, 1974] or Schwarz Bayesian Criterion (SBC) [*Schwarz*, 1978]. The AIC and SBC values are derived from the generalized Akaike information criterion (GAIC) for each tested distribution:

$$\mathrm{GAIC} = -2\hat{\ell} + p \cdot df \tag{2}$$

where $\hat{\ell}$ is the maximized value of the log-likelihood function, p is a penalty factor ($p = 2$ for AIC and $p = \ln(n)$ for SBC, where n is the number of observations), and df is the number of degrees of freedom (number of free parameters of the studied distribution). The AIC and SBC are thus measures of the trade-off between closeness of fitting (higher $\hat{\ell}$) and complexity (larger number of parameters). Distribution selection with the SBC, which has a more severe penalty for increasing the degrees of freedom, results in a simpler model (i.e., fewer parameters) than that selected by AIC. The use of the SBC for selecting models prevents model overfitting, i.e., when the number of parameters is too large relative to the number of observation. At equal maximized log-likelihood $\hat{\ell}$ amongst the five tested distributions, the exponential distribution is thus favored by the AIC (and even more by the SBC) criterion as it has only one parameter, and the power exponential which has three parameters is the most penalized (also even more penalized by the SBC). The difference ($\Delta(\mathrm{AIC}_k) = \mathrm{AIC}_k - \mathrm{AIC}_{\mathrm{min}}$) between the lowest AIC ($\mathrm{AIC}_{\mathrm{min}}$) and the AIC_k values of an alternative distribution k increases as the goodness of fit of the distribution k decreases. We considered that models with $\Delta(\mathrm{AIC}_k) < 5$ have substantial support based on the full theoretical analysis of *Burnham and Anderson* [2002].

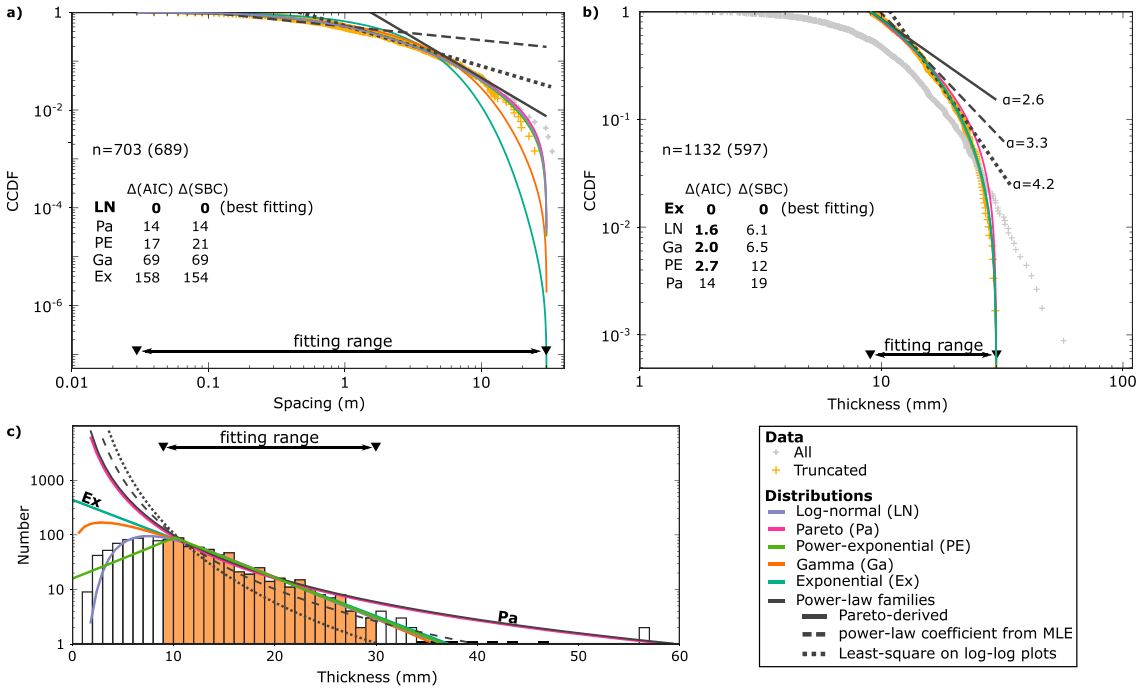

Figure 6. Estimations of the probability distribution of fracture attributes. (a) Complementary CDF (CCDF) of the spacing data of fracture set 1 in all three boreholes combined and fitted distributions. (b) CCDF of fracture thickness data for all fractures and fitted distributions. *n* is the total number of fractures in the data set, truncated number within brackets. Δ(AIC) and Δ(SBC) are indicated for all distributions, with those distributions satisfying Δ(AIC) or Δ(SBC)<5 are in bold. (c) Histogram of all measured fracture thickness in log-linear scale, with the probability density functions of distributions fitted over the 9–30 mm scale range, extended over the entire range of observation. In this coordinate system, the exponential distribution plots as a straight line.

The histogram $h^n(x|\Theta)$ of n values having a probability distribution $f(x|\Theta)$ is $h^n(x|\Theta) = n \cdot f(x|\Theta)$. For distributions evaluated within a truncated range, the extrapolation of the histogram out of truncation bounds is calculated with

$$h^{Ntot}(x|\hat{\Theta}) = \frac{N_{tr}}{F(x_2|\hat{\Theta}) - F(x_1|\hat{\Theta})} \cdot f_{tr}(x|\hat{\Theta}) = N_{tot} \cdot f_{tr}(x|\hat{\Theta}) \quad (3)$$

where $f_{tr}(x|\hat{\Theta})$ is the probability density function estimated within truncated range with a series of estimated parameters $\hat{\Theta}$; N_{tot} is the total number of fractures assuming there were no truncations, calculated from the number of samples occurring within the truncated range (N_{tr}) and the cumulative density function (CDF) of the non truncated distribution $F(x|\hat{\Theta})$ evaluated on the lower (x_1) and upper (x_2) truncation limits. The functions f and f_{tr} have the same form and parameters.

4.4. Distribution Fitting Example

Figure 6a shows an example of fitting of the five distributions considered for the spacing of the dominant fracture set ("1") in all three boreholes combined. In this case, the lognormal distribution fits the data best, and there are no other close contenders (i.e., $\Delta(AIC_i)$ and $\Delta(SBC_i) > 5$ for all other distributions). Visually, the exponential and gamma distributions do not fit the data well, but it would not be possible to rule out the Pareto and power-exponential distributions. None of the power law-type distributions fit the data well, with coefficients of 1.3 (MLE estimation of power law coefficient), 1.8 (least squares regression in log-log plot), and 2.6 (derived from the Pareto distribution), a wide range which encompasses most values found in geological systems (1 to ~3 [*Bonnet et al.*, 2001]).

In some cases, several distributions yield similarly good fits to the data. For example, the exponential distribution has the best fit for fracture thickness ($AIC = AIC_{min}$), but all other distributions with the exception of

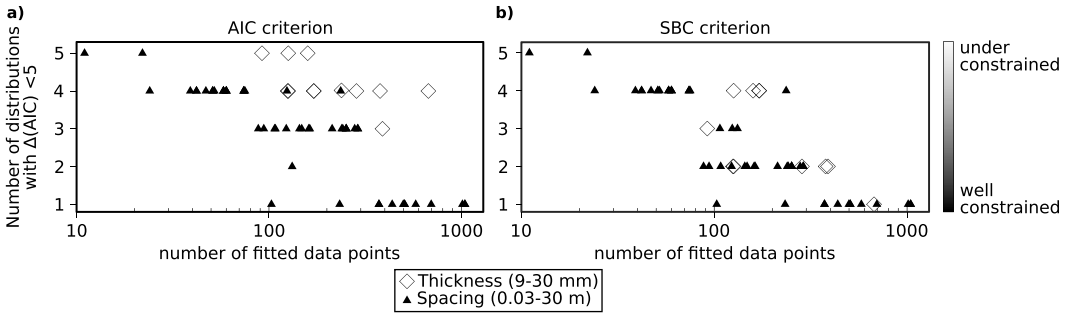

Figure 7. Number of distributions satisfying the AIC and SBC conditions as a function of the input number of data points, for the fracture thickness (fitted between 9 and 30 mm) and the fracture spacing (fitted between 0.03 and 30 m). (a) AIC condition. (b) SBC condition.

Pareto are just as good according to the AIC criterion with $\Delta(AIC_i)$ ranging from 1.6 to 2.7 (Figure 6b). The thickness data set spans only half an order of magnitude and is therefore not as well constrained as the spacing data set which spans 3 orders of magnitude. Because of the limited scale range, a conservative interpretation with the SBC, which in the case of thickness evaluation selects only the distribution with a single parameter (exponential), is preferred to the results suggested by the AIC to limit overfitting.

As an example of distributions fitted over a truncated range and extrapolated beyond the truncation bounds, a histogram of fracture thickness has been plotted in Figure 6c. All distributions fitted with GAMLSS exhibit a good visual fit to the histogram between the truncation bounds but have different trends outside the bounds. The power law distributions estimated by MLE (via Pareto and from MLE estimation of the power law coefficient) have a good visual fit to the histogram, but the power law with the exponent estimated by least squares on a log-log plot does not.

4.5. How Many Fractures Are Enough?

The number of distributions satisfying the AIC and SBC conditions ($\Delta(AIC)$ or $\Delta(AIC) < 5$) depends on both the scale range (interval within truncation limits) and size (number of input data points) of the input data set. To quantify this dependency, the statistical analysis is made on a series of subsets of different sizes (for different fracture sets) and scale ranges of attribute values (thickness and spacing), resulting in a varying number of distributions with $\Delta(AIC) < 5$ (Figure 7a) or $\Delta(SBC) < 5$ (Figure 7b). The number of distributions satisfying the AIC condition varies from 1 to 4 for 80 to 300 fractures, which relates to how well the measurements follow a theoretical probability distribution. For the spacing analysis evaluated over 3 orders of magnitude (0.03–30 m), models with fewer than 80 fractures have either four or five models satisfying $\Delta(AIC) < 5$ and are underconstrained, whereas data sets with >300 fractures are better constrained with only one distribution with $\Delta(AIC) < 5$ (Figure 7a).

The spacing data set spanning a large-scale range (3 orders of magnitude) has fewer models satisfying the AIC and SBC conditions than the thickness data set which spans only half on order of magnitude. The AIC condition is satisfied for three or four distributions even for thickness data sets containing more than 300 fractures. The SBC condition is satisfied by fewer distributions than the AIC because the SBC further penalizes distributions with several parameters.

The location of the range of observations considered to be fully sampled also affects the number of distributions satisfying the AIC or SBC conditions. Tests were performed on a series of fracture spacing data sets for a single fracture set spanning 2 orders of magnitude, with different truncation limits (0.01–1 m, 0.05–5 m, 0.1–10 m, 0.5–50 m, and 1–100 m). While the best fitting distribution amongst the five tested is always lognormal, other distributions (power-exponential, gamma, and Pareto) satisfy the AIC condition for some of the subsets (Figure 8a). In addition, although the data are truncated in reality, we fit a distribution to the whole data set without limitations on the model or the data. In this case, only the lognormal distribution satisfies the AIC condition (Figure 8b), which reflects the higher number of input data. In addition, the lognormal

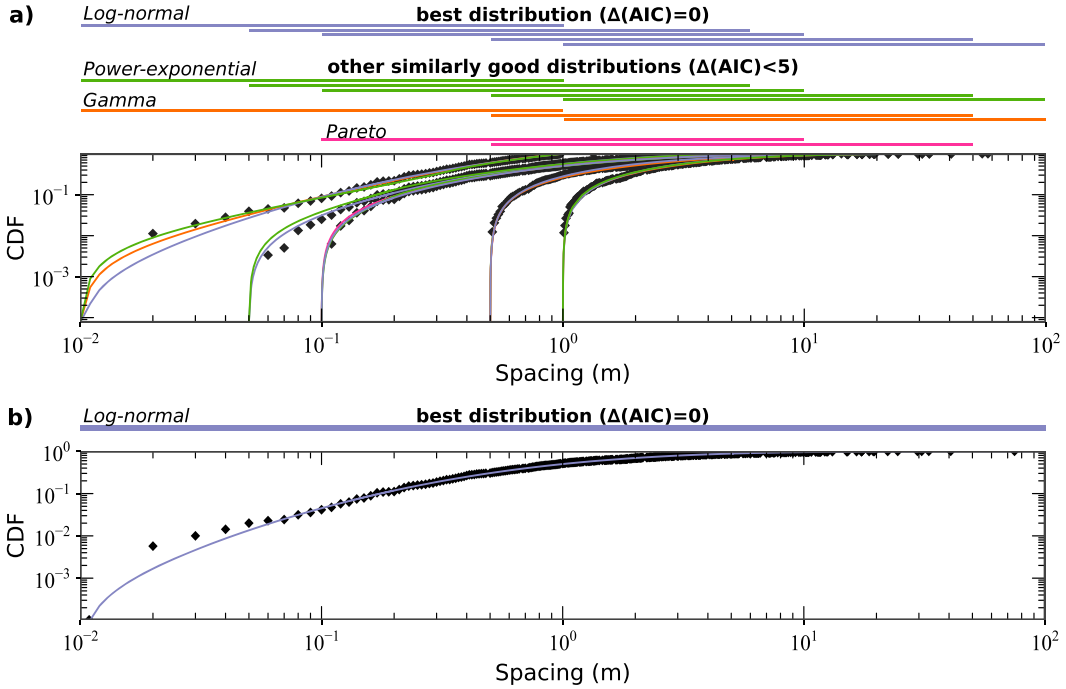

Figure 8. Effect of the location of truncating limits on the number and form of best distributions (Δ(AIC)<5) fitting the fracture spacing of fracture set 1 in all boreholes. (a) CDF of fracture spacing for different truncation intervals each covering 2 orders of magnitude. In several cases, fitted distributions are naturally superposed. (b) CDF of fracture spacing for the whole range of measured values. The distributions with Δ(AIC)<5 are displayed on each corresponding CDF of the data and as bars at the top of each plot.

distribution approximates well the undersampled lower tail of the measurements. Defining the truncation limits of a data set prior to fitting is thus particularly important, as a lognormal (or gamma) distribution may reflect not simply the distribution of the geological data but also sampling effects and truncations.

5. Discussion

5.1. Statistical Analysis of Fractures Interpreted in BHTV Logs

BHTV logs are similar to a scanline sampling in that they measure the orientation and morphological characteristics of fractures intersecting a line, and standard analysis methods are applicable [e.g., *Priest*, 1993]. However, a number of precautions must be taken to accommodate particular artifacts and resolution issues, and to enable reliable fracture data set interpretations.

The BHTV log quality is affected by a number of logging and drilling artifacts, which can affect the statistical analysis of fracture attributes. The log quality is affected by the type of logging tool used. At Rotokawa, the high-temperature ABI-85 tool had a lower resolution (5×5 mm) than other standard tools, at the times the logs were acquired. In addition, some signal was commonly lost in parts of the borehole due to spalling from the borehole wall on the high side of the deviated boreholes and in possible intensely fractured areas (where fracture spacing would have been lower than the truncation limit). Finally, the andesitic rocks imaged by the BHTV logs at Rotokawa are likely to have a high roughness at the borehole wall, which decreases the amplitude of the returned signal and thus the ability to detect signal related to fractures within the noise. As the statistical analysis of fracture thickness and spacing is highly dependent on the scale range of observations, where the data are fully observed (within truncation limits), it is important to evaluate image quality effects in each BHTV log.

The estimated fracture thickness, although corrected for the intersection angle with the borehole, is overestimated due to erosion of the fracture at the borehole wall. Some types of fractures may also be particularly subject to increased erosion, such as those infilled with clay or other weak material.

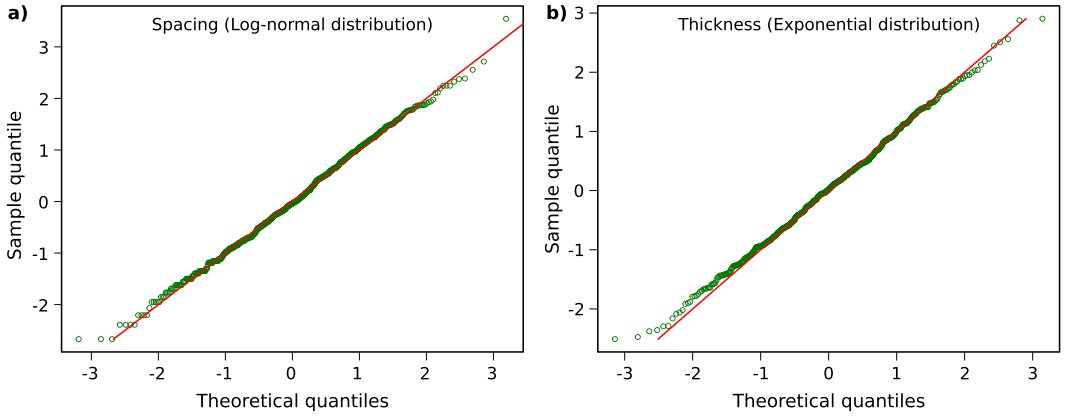

Figure 9. Examples of Q-Q plots of fitted distributions; a good alignment between the sample and theoretical quantiles on the line $y = x$ (red line) indicates a good fit. (a) Lognormal distribution of spacing in fracture set 1 in all wells (Figure 6a). (b) Exponential distribution of thickness in all wells (Figure 6b).

Some types of fractures may exhibit a similar acoustic amplitude response to that of the host formation, depending on their mineralization, and are thus difficult to detect on BHTV logs. In addition, planar features may consist of lithological features (e.g., bedding and foliation) rather than fractures. While such detection issues were not deemed to be serious in the Rotokawa BHTV logs, they could have an effect on the fracture detection and subsequent statistical analysis in other situations. Comparison of BHTV log with cores or other geophysical logs [*Genter et al.*, 1997], unavailable in the Rotokawa BHTV logs, would help resolving this issue.

The Terzaghi correction for orientation sampling bias improves the delineation of fracture sets but does not rectify the lack of fractures subparallel to the borehole (< 10°; Figure 3). As with measurements of fractures along scanlines of different orientations spanning the same outcrop, a combination of boreholes drilled in different directions permits the sampling of all fracture sets. For example, the clustering analysis conducted here highlighted the possible presence of a fourth fracture set that had not been identified previously. This fracture set "4," which appears to be linked to an orientation sampling bias in boreholes RK18L2 and RK32, forms a separate cluster in RK30L1 in a direction not affected by the orientation bias and produces clustering configurations with high *K*-means silhouette width (Figure A1). The orientation of fracture set 4 is consistent with the presence of normal faults of Andersonian orientations (dipping 60° and striking parallel to S_{Hmax}), which are to be expected in the Rotokawa geological setting. However, the assumption that fracture orientations are similar in each borehole is not always applicable, due, for example, to the presence of active faults that may locally change the in situ stress and the resulting fracture orientations [*McNamara et al.*, 2015], or to different structural compartments within which fracture orientations vary laterally or with depth. For example fracture set "3" is observed in one borehole (RK30L1) but very rarely in the two others available in this study, which suggests that fractures of this orientation are not present homogeneously throughout the reservoir.

5.2. Uncertainties and Multiple "Best" Solutions

The clustering of fracture orientation and the statistical analyses of fracture thickness and spacing both reveal that several "best fits" often occur. There are at least two good clustering configurations of fracture orientations for each borehole and the combined data set (Appendix A). Comparisons between several fracture set delineation techniques (Fisher contours, *K*-means, fuzzy *K*-means, and agglomerative clustering) highlight different possible solutions for a single data set. The agreement between different techniques, in the context of relevant geological setting, provides the best delineation of fracture sets.

The maximum likelihood estimation method, combined with the AIC and SBC, is able to identify the distribution best approximating a data set amongst a given set of distributions, as well as other distributions that also have similarly good fits to the data. The restricted range of observations for fracture thickness limits the ability

to identify a single best fit distribution. Even for the spacing analysis which has a wider range of observations (3 orders of magnitude), a minimum of 100 data points is necessary to identify the distribution that fits the data set significantly better than all other tested distributions. At Rotokawa, 1218 fractures were identified in the BHTV logs, but the sampling biases and variable BHTV log quality reduce the number of fractures usable for statistical analysis. In addition, the requirements of studying each fracture set individually divides the data set into subsets, sometimes too small to identify the type of distribution they follow.

The ranking of the likelihood of a distribution using the AIC and SBC is relative and does not guarantee that the data follow one of the models, so it is important to test different distributions relevant to the type of studied data. Goodness-of-fit tests such as Chi-squared or Kolmogorov-Smirnov tests may be used [*James et al.*, 2013], particularly if fitting only one or two distributions. In this study, however, the objective of the statistical analysis is to evaluate which of the probability distributions commonly found in geological settings best fit the data for further geological interpretation and fracture modeling. As such, a relative ranking of these distributions most commonly encountered in geological settings is sufficient. However, we have also ensured that the distributions with $\Delta(\mathrm{AIC}) < 5$ have good fits to the data (i.e., absolute rather than relative best fit) by inspecting Q-Q plots (Figure 9). When several distributions satisfy the AIC and SBC conditions, additional data sets covering different scales are required to decide which distribution best approximates the attribute [*McCaffrey et al.*, 2003; *Torabi and Berg*, 2011]. For example, combining BHTV log thickness data with measurements of millimeter thick (or smaller) fractures in drill cores would help constrain which of the exponential, lognormal, or even power law distributions best represent the fracture thickness population over its entire range (see companion paper *Massiot et al.* [2017]).

Given the uncertainties associated with the statistical analysis of fracture thickness and spacing, it is desirable to consider several scenarios which each fit the data in order to describe the fracture system, rather than a single configuration.

5.3. Multivariate Analysis

Maximum likelihood estimation of the distribution of fracture attributes using truncated distributions, presented here for thickness and spacing, is applicable to other fracture attributes such as length. In this paper, the analyses of orientation, thickness, and spacing are made independently. However, the delineation of fracture sets using a combination of fracture attributes measured on scanlines (e.g., orientation, length, spacing, and roughness) can better characterize the fracture system than when using orientation alone as shown by, for example, *Tokhmechi et al.* [2011] and *Hofrichter and Winkler* [2006] in engineering and fractured reservoirs applications, respectively. Such multivariate classifications may be applicable to BHTV log measurements in high-temperature geothermal reservoirs, as correlations were found between permeability and cross-cutting fractures interpreted from BHTV logs at the Kawerau geothermal field, Taupo Volcanic Zone [*Wallis et al.*, 2012]. Classifications of fracture attributes measured on scanlines have previously been made using *K*-means [*Tokhmechi et al.*, 2011] and fuzzy *K*-means clusterings [*Hammah and Curran*, 1998], neural networks [*Sirat and Talbot*, 2001], and Parzen classifiers [*Tokhmechi et al.*, 2011], the latter two using training and testing subsets of the whole data sets. BHTV logs do not provide as detailed information of fracture attributes as scanlines (e.g., length, roughness, and infilling). However, other types of wireline logs can be jointly interpreted with fracture data set interpreted in BHTV logs, using principal component analysis to identify lithologies [*Townend et al.*, 2013] or fuzzy logic to identify permeable zones in oil boreholes [*Masoudi et al.*, 2012]. In these cases, the distance measure ("dissimilarity") has to be compatible between orientation data, continuous data (e.g., position along boreholes and thickness [*Hammah and Curran*, 1999]), categorical data (e.g., cross-cutting relationships and rock type), and other wireline log data sampled at different resolutions, with relative weightings appropriate to the studied parameters.

6. Conclusion

BHTV logs provide near-continuous records of fracture geometrical characteristics at depth. The application of clustering algorithms extends the fracture orientation analysis made by analysts using stereonets, by providing transparent classifications of fracture orientations into distinct groups, and metrics with which to choose the most appropriate number of clusters. Maximum likelihood estimation (MLE) methods applied to truncated

distributions are suitable for evaluating the distribution of fracture attributes (presented here for spacing and thickness) affected by sampling biases. The AIC and SBC are simple tools with which to select distributions best representing the data over the truncated range, amongst a set of distribution forms. Distributions evaluated within truncation ranges where they are deemed fully sampled can then be extrapolated over the whole range of values of the studied attribute. A suitable level of BHTV log quality also needs to be assessed to limit the effects of sampling bias on fracture attribute analysis. Depending on the number of input fracture data and the range of values they cover (in both size and location), AIC and SBC may rank more than one distribution as similarly good approximations of the data. This statistical approach to fracture attribute analysis, presented here for orientation, thickness, and spacing, and also applicable to other attributes, provides a series of realistic approximations which can be used to constrain reservoir-scale fracture models.

Appendix A: Evaluation of the Cluster Number for Each Borehole

Figure A1 presents the metrics used to choose the best clustering of fracture orientation interpreted in the three boreholes and the combined data set comprising data from all three boreholes.

Appendix B: Probability Distribution Formulas

Table B1 details the formulas of the probability distributions used in this paper.

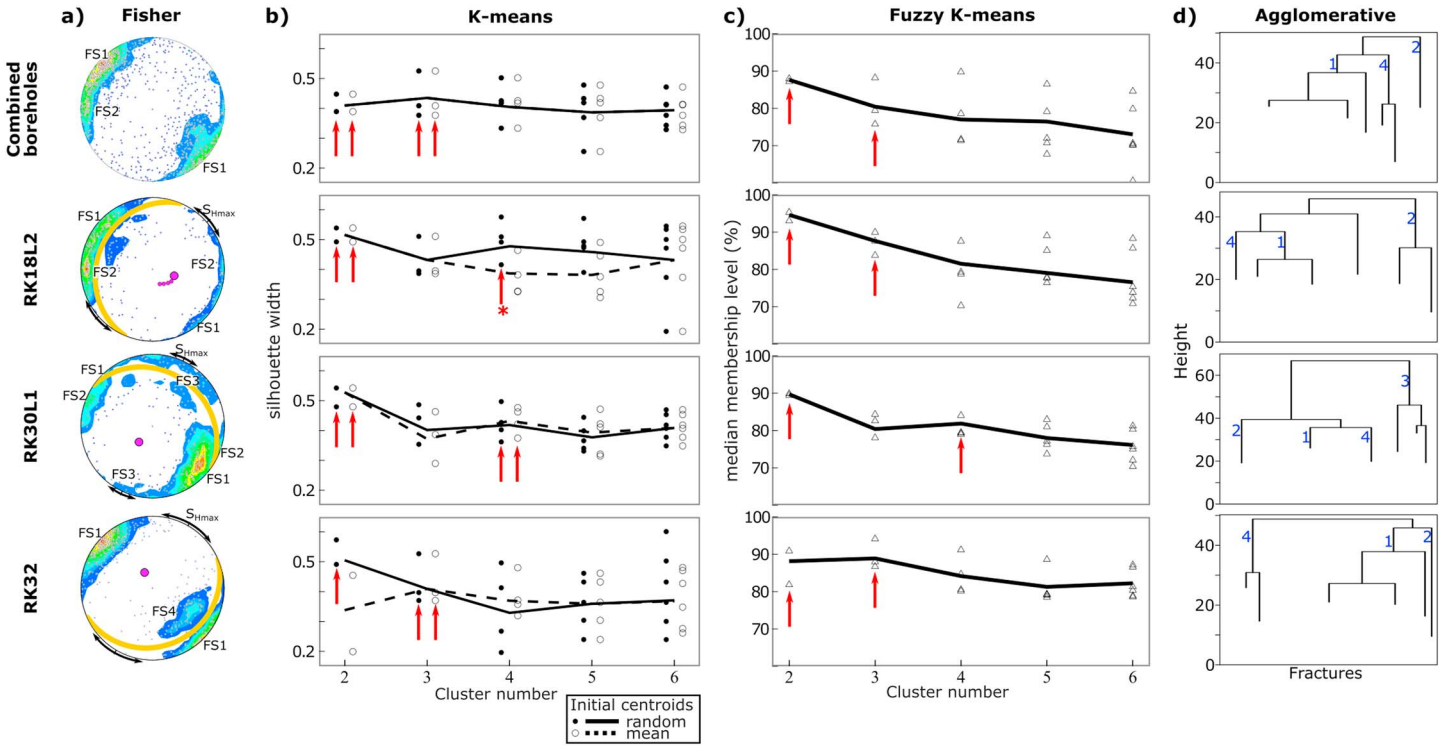

Figure A1. Evaluation of the optimal number of cluster for each of the three boreholes and combined. (a) Fisher contouring (percentages) of poles to fracture planes with resulting fracture sets (FS), S_{Hmax} orientation (mean value and one standard deviation [*McNamara et al.*, 2015]), and great circle with the orientation of poles to planes of fractures not sampled because they are parallel to the borehole (the pole of this great circle is the borehole trajectory). Stereonets are displayed as lower hemisphere Schmidt projection. (b) *K*-means: average silhouette width for each cluster (dots) and average of the average silhouette widths (line) for each number of clusters; clusterings are made with random initial centroids and initial centroids located at the mean orientation of the fracture set. (c) Fuzzy *K*-means: median membership level for each cluster (triangle) and median membership level (line) for each number of clusters. (d) Dendogram representing the agglomerative clustering, with the level at which each of the four main fracture sets emerge. The best clusterings are indicated by the underlying arrows in Figures A1b and A1c; best clusterings with either three (combined borehole and borehole RK32) or four (boreholes RK18L2 and RK30L1) clusters separate fracture set "4" from fracture set "1," striking NE-SW and dipping ~ 60° and ~ 80°, respectively.

Table B1. Probability Density Function Formulas of Distributions Used in This Paper and Conversions From GAMLSS Formulations to Other Common Formulations[a]

Distribution	Probability Density Function Formulations	Conversion
Exponential	$f_y(y\|\mu)$[b] $= \frac{1}{\mu}\exp\left(-\frac{1}{\mu}y\right)$	$\lambda = \frac{1}{\mu}$
	$f_y(y\|\lambda) = \lambda\exp(-\lambda y)$	
Gamma	$f_y(y\|\mu,\sigma)$[b] $= \frac{y^{\left(\frac{1}{\sigma^2}-1\right)}\exp\left[-\frac{y}{\sigma^2\mu}\right]}{(\sigma^2\mu)^{\frac{1}{\sigma^2}}\Gamma\left(\frac{1}{\sigma^2}\right)}$	$a = \frac{1}{\sigma^2}$; $s = \sigma^2\mu$
	$f_y(y\|a,s) = \frac{1}{s^a\Gamma(a)}y^{(a-1)}\exp[-(y/s)]$	
Lognormal	$f_y(y\|\mu,\sigma) = \frac{1}{y\sqrt{2\pi}\sigma}\exp\left[-\frac{1}{2}(\frac{\log y-\mu}{\sigma})^2\right]$	
Pareto[b]	$f_y(y\|\mu,\sigma)$[b] $= \frac{1}{\sigma}\mu^{\frac{1}{\sigma}}(y+\mu)^{-\left(\frac{1}{\sigma}+1\right)}$	$\alpha = \left(\frac{1}{\sigma}+1\right)$ for $\mu << y$
Power law	$f_y(y\|\alpha) = C * y^{-\alpha}$ for $\alpha > 1$	
	α estimated by least squares regressions in log-log plots, and by MLE following *Clauset et al.* [2009]:	
	$\alpha = 1 + n\left[\sum_{i=1}^{n}\frac{y_i}{y_{\min}}\right]^{-1}$, $y_i > y_{\min}$	
Power-exponential	$f_y(y\|\mu,\sigma,\nu)^* = \frac{\frac{1}{\sigma}(\nu\exp[-0.5\|z/c\|^\nu])}{c.2^{1+\frac{1}{\nu}}\Gamma\left(\frac{1}{\nu}\right)}$ where $c = \left[\frac{2^{-\frac{2}{\nu}}\Gamma\left(\frac{1}{\nu}\right)}{\Gamma\left(\frac{3}{\nu}\right)}\right]^{0.5}$	
	$f_y(y\|\beta,\lambda,y_{\min}) = \beta\lambda\exp[\lambda y_{\min}^{\beta}]y^{\beta-1}\exp[-\lambda y^{\beta}]$	

[a]The GAMLSS lognormal distribution formulation is the common formulation. All variable (y) and parameters (μ, σ, and ν) are strictly positive, except for μ of the lognormal and power-exponential distributions.
[b]GAMLSS formulations.

Acknowledgments
We thank Euan G.C. Smith and Richard Arnold for their constructive advice. Comments from Nicholas Davatzes, Julie Rowland, and Martha Savage also improved this manuscript. This project forms part of the first author's PhD thesis funded by the Sarah Beanland Memorial Scholarship awarded by GNS Science. Additional support was provided by the GNS Science's "Geothermal Resources of New Zealand" research program. The authors thank the Rotokawa Joint Venture (Mercury New Zealand and Tauhara North No.2 Trust) for allowing publication of this work. We thank Colleen Barton and Ken McCaffrey for their constructive reviews of this work. Data used in this manuscript are available with the companion manuscript [*Massiot et al.*, 2017].

References

Agosta, F., M. Alessandroni, M. Antonellini, E. Tondi, and M. Giorgioni (2010), From fractures to flow: A field-based quantitative analysis of an outcropping carbonate reservoir, *Tectonophysics*, *490*(3-4), 197–213, doi:10.1016/j.tecto.2010.05.005.

Akaike, H. (1974), A new look at the statistical model identification, *IEEE Trans. Autom. Control*, *19*(6), 716–723, doi:10.1109/tac.1974.1100705.

Ásmundsson, R., et al. (2014), High temperature instruments and methods developed for supercritical geothermal reservoir characterisation and exploitation—The HiTI project, *Geothermics*, *49*, 90–98, doi:10.1016/j.geothermics.2013.07.008.

Barton, C. A., and M. D. Zoback (1992), Self-similar distribution and properties of macroscopic fractures at depth in crystalline rock in the Cajon Pass Scientific Drill Hole, *J. Geophys. Res.*, *97*(B4), 5181–5200, doi:10.1029/91JB01674.

Berkowitz, B. (2002), Characterizing flow and transport in fractured geological media: A review, *Adv. Water Resour.*, *25*(8-12), 861–884, doi:10.1016/s0309-1708(02)00042-8.

Bonneau, F., V. Henrion, G. Caumon, P. Renard, and J. Sausse (2013), A methodology for pseudo-genetic stochastic modeling of discrete fracture networks, *Comput. Geosci.*, *56*, 12–22, doi:10.1016/j.cageo.2013.02.004.

Bonnet, E., O. Bour, N. E. Odling, P. Davy, I. Main, P. Cowie, and B. Berkowitz (2001), Scaling of fracture systems in geological media, *Rev. Geophys.*, *39*(3), 347–383, doi:10.1029/1999RG000074.

Burnham, K. P., and D. R. Anderson (2002), *Model Selection and Multimodel Inference: A Practical Information-Theoretic Approach*, 2nd ed., Springer, New York.

Clauset, A., C. R. Shalizi, and M. E. J. Newman (2009), Power-law distributions in empirical data, *Soc. Indust. Appl. Math. Rev.*, *51*(4), 661–703, doi:10.1137/070710111.

Dershowitz, W. S., and H. H. Einstein (1988), Characterizing rock joint geometry with joint system models, *Rock Mech. Rock Eng.*, *21*, 21–51, doi:10.1007/BF01019674.

Dezayes, C., C. Lerouge, B. Sanjuan, C. Ramboz, and M. Brach (2015), Toward a better understanding of the fluid circulation in the rhine graben for a better geothermal exploration of the deep basins, paper presented at World Geothermal Congress, Melbourne, Australia, 19–25 April.

Genter, A., and H. Traineau (1996), Analysis of macroscopic fractures in granite in the HDR geothermal well EPS-1, Soultz-sous-Forêts, France, *J. Volcanol. Geotherm. Res.*, *72*(1-2), 121–141, doi:10.1016/0377-0273(95)00070-4.

Genter, A., C. Castaing, C. Dezayes, H. Tenzer, H. Traineau, and T. Villemin (1997), Comparative analysis of direct (core) and indirect (borehole imaging tools) collection of fracture data in the Hot Dry Rock Soultz reservoir (France), *J. Geophys. Res.*, *102*(B7), 15,419–15,431, doi:10.1029/97JB00626.

Gillespie, P., C. Howard, J. Walsh, and J. Watterson (1993), Measurement and characterisation of spatial distributions of fractures, *Tectonophysics*, *226*(1-4), 113–141, doi:10.1016/0040-1951(93)90114-y.

Guerriero, V., S. Vitale, S. Ciarcia, and S. Mazzoli (2011), Improved statistical multi-scale analysis of fractured reservoir analogues, *Tectonophysics*, *504*(1-4), 14–24, doi:10.1016/j.tecto.2011.01.003.

Hammah, R., and J. Curran (1998), Fuzzy cluster algorithm for the automatic identification of joint sets, *Int. J. Rock Mech. Min. Sci.*, *35*(7), 889–905, doi:10.1016/s0148-9062(98)00011-4.

Hammah, R. E., and J. H. Curran (1999), On distance measures for the fuzzy *K*-means algorithm for joint data, *Rock Mech. Rock Eng.*, *32*(1), 1–27, doi:10.1007/s006030050041.
Hofrichter, J., and G. Winkler (2006), Statistical analysis for the hydrogeological evaluation of the fracture networks in hard rocks, *Environ. Geol.*, *49*(6), 821–827, doi:10.1007/s00254-006-0177-5.
James, G., D. Witten, T. Hastie, and R. Tibshirani (2013), *An Introduction to Statistical Learning*, Springer, New York.
Laslett, G. M. (1982), Censoring and edge effects in areal and line transect sampling of rock joint traces, *J. Int. Assoc. Math. Geol.*, *14*(2), 125–140, doi:10.1007/bf01083948.
Li, Y., Q. Wang, J. Chen, L. Xu, and S. Song (2014), K-means algorithm based on particle swarm optimization for the identification of rock discontinuity sets, *Rock Mech. Rock Eng.*, *48*, 375–385, doi:10.1007/s00603-014-0569-x.
Lofts, J. C., and L. T. Bourke (1999), The recognition of artefacts from acoustic and resistivity borehole imaging devices, *Geol. Soc. London, Spec. Publ.*, *159*, 59–76, doi:10.1144/gsl.sp.1999.159.01.03.
Masoudi, P., B. Tokhmechi, M. Jafari, and B. Moshiri (2012), Application of fuzzy classifier fusion in determining productive zones in oil wells, *Energy Explor. Exploit.*, *30*(3), 403–415, doi:10.1260/0144-5987.30.3.403.
Massiot, C., D. McNamara, and B. Lewis (2015), Processing and analysis of high temperature geothermal acoustic borehole image logs in the Taupo Volcanic Zone, New Zealand, *Geothermics*, *53*, 190–201, doi:10.1016/j.geothermics.2014.05.010.
Massiot, C., A. Nicol, D. D. McNamara, and J. Townend (2017), Evidence for tectonic, lithologic and thermal controls on fracture system geometries in an andesitic high-temperature geothermal field, *J. Geophys. Res. Solid Earth*, *122*, doi:10.1002/2017JB014121.
McCaffrey, K. J. W., J. M. Sleight, S. Pugliese, and R. E. Holdsworth (2003), Fracture formation and evolution in crystalline rocks: Insights from attribute analysis, *Geol. Soc. London Spec. Publ.*, *214*(1), 109–124, doi:10.1144/gsl.sp.2003.214.01.07.
McNamara, D. D., C. Massiot, B. Lewis, and I. C. Wallis (2015), Heterogeneity of structure and stress in the Rotokawa Geothermal Field, New Zealand, *J. Geophys. Res. Solid Earth*, *120*, 1243–1262, doi:10.1002/2014JB011480.
McNamara, D. D., S. Sewell, E. Buscarlet, and I. C. Wallis (2016), A review of the Rotokawa Geothermal Field, New Zealand, *Geothermics*, *59*(B), 281–293, doi:10.1016/j.geothermics.2015.07.007.
Milloy, S. F., K. Mclean, and D. D. McNamara (2015), Comparing borehole televiewer logs with continuous core: An example from New Zealand, paper presented at World Geothermal Congress, Melbourne, Australia, 19–25 April.
Newman, M. (2005), Power laws, Pareto distributions and Zipf's law, *Contemp. Phys.*, *46*(5), 323–351, doi:10.1080/00107510500052444.
Nicol, A., J. Walsh, J. Watterson, and P. Gillespie (1996), Fault size distributions—Are they really power-law?, *J. Struct. Geol.*, *18*(2-3), 191–197, doi:10.1016/s0191-8141(96)80044-7.
Pickering, G., J. Bull, and D. Sanderson (1995), Sampling power-law distributions, *Tectonophysics*, *248*(1-2), 1–20, doi:10.1016/0040-1951(95)00030-q.
Poppelreiter, M., C. Garcia-Carballido, and M. Kraaijveld (Eds.) (2010), *Dipmeter and Borehole Image Log Technology: AAPG Memoir 1992*, 1st ed., 357 pp., AAPG, Tulsa, Okla.
Priest, S. D. (1993), *Discontinuity Analysis for Rock Engineering*,Springer, Netherlands, doi:10.1007/978-94-011-1498-1.
R Core Team (2015), *R: A Language and Environment for Statistical Computing*, R Found. for Stat. Comput., Vienna.
Reynolds, A. P., G. Richards, B. de la Iglesia, and V. J. Rayward-Smith (2006), Clustering rules: A comparison of partitioning and hierarchical clustering algorithms, *J. Math. Model. Algorit.*, *5*(4), 475–504, doi:10.1007/s10852-005-9022-1.
Schöpfer, M. P., A. Arslan, J. J. Walsh, and C. Childs (2011), Reconciliation of contrasting theories for fracture spacing in layered rocks, *J. Struct. Geol.*, *33*(4), 551–565, doi:10.1016/j.jsg.2011.01.008.
Schwarz, G. (1978), Estimating the dimension of a model, *Ann. Stat.*, *6*(2), 461–464, doi:10.1214/aos/1176344136.
Seebeck, H., A. Nicol, P. Villamor, J. Ristau, and J. Pettinga (2014), Structure and kinematics of the Taupo Rift, New Zealand, *Tectonics*, *33*(6), 1178–1199, doi:10.1002/2014tc003569.
Shanley, R. J., and M. A. Mahtab (1976), Delineation and analysis of clusters in orientation data, *J. Int. Assoc. Math. Geol.*, *8*(1), 9–23, doi:10.1007/bf01039681.
Sirat, M., and C. J. Talbot (2001), Application of artificial neural networks to fracture analysis at the Äspö HRL, Sweden: Fracture sets classification, *Int. J. Rock Mech. Min. Sci.*, *38*(5), 621–639, doi:10.1016/S1365-1609(01)00030-2.
Stasinopoulos, D. M., and R. A. Rigby (2007), Generalized Additive Models for Location Scale and Shape (GAMLSS) in R, *J. Stat. Software*, *23*(7), 1–46, doi:10.18637/jss.v023.i07.
Terzaghi, R. D. (1965), Sources of error in joint surveys, *Géotechnique*, *15*(3), 287–304, doi:10.1680/geot.1965.15.3.287.
Tokhmechi, B., H. Memarian, B. Moshiri, V. Rasouli, and H. A. Noubari (2011), Investigating the validity of conventional joint set clustering methods, *Eng. Geol.*, *118*(3-4), 75–81, doi:10.1016/j.enggeo.2011.01.002.
Torabi, A., and S. S. Berg (2011), Scaling of fault attributes: A review, *Mar. Pet. Geol.*, *28*(8), 1444–1460, doi:10.1016/j.marpetgeo.2011.04.003.
Townend, J., R. Sutherland, V. G. Toy, J. D. Eccles, C. Boulton, S. C. Cox, and D. McNamara (2013), Late-interseismic state of a continental plate-bounding fault: Petrophysical results from DFDP-1 wireline logging and core analysis, Alpine Fault, New Zealand, *Geochem. Geophys. Geosyst.*, *14*(9), 3801–3820, doi:10.1002/ggge.20236.
Villaescusa, E., and E. T. Brown (1992), Maximum likelihood estimation of joint size from trace length measurements, *Rock Mech. Rock Eng.*, *25*(2), 67–87, doi:10.1007/BF01040513.
Wallis, I. C., D. McNamara, J. V. Rowland, and C. Massiot (2012), The nature of fracture permeability in the basement greywacke at Kawerau Geothermal Field, New Zealand, paper presented at the 37th Workshop on Geothermal Reservoir Engineering, Stanford Univ., Stanford, Calif., 30 January–February.
Zadeh, L. (1965), Fuzzy sets, *Inf. Control*, *8*(3), 338–353, doi:10.1016/s0019-9958(65)90241-x.
Zemanek, J., E. E. Glenn, L. J. Norton, and R. L. Caldwell (1970), Formation evaluation by inspection with the borehole televiewer, *Geophysics*, *35*(2), 254–269, doi:10.1190/1.1440089.
Zhou, W., and N. H. Maerz (2002), Implementation of multivariate clustering methods for characterizing discontinuities data from scanlines and oriented boreholes, *Comput. Geosci.*, *28*(7), 827–839, doi:10.1016/s0098-3004(01)00111-x.
Zuquim, M., and J. V. Rowland (2013), Structural controls on fluid flow at the Onemana area, Coromandel Peninsula, New Zealand, paper presented at the 35th NZ Geothermal Workshop, Rotorua, New Zealand 17–20 Nov.